JOURNAL OF AIRCRAFT
Vol. 29, No. 4, July–Aug. 1992

Simulation of Transonic Flow over Twin-Jet Transport Aircraft

S. Rill* and K. Becker†
Deutsche Airbus GmbH, Bremen, Germany

The capability of the grid generation/Euler solver combination to simulate transonic flows over twin-jet transport aircraft is demonstrated. The numerical simulation is based on MELINA, an explicit, multiblock, structured-mesh, Runge-Kutta scheme, and the interactive, algebraic grid generation system INGRID. The problems of complex transport aircraft geometry (body/wing/flap-track-fairings/pylon and engine) and of jet or nacelle flow are tackled, yielding an efficient, robust, and accurate flow simulation system. The prediction of engine installation effects are validated with wind-tunnel experiments for two different transport aircraft configurations with under-wing, pylon-mounted turbo fan engines. From the validation it can be concluded that the numerical simulation has approached a level of accuracy and efficiency where it can be used to investigate and optimize under-wing, pylon-mounted engine installations already at an early project state and reduce development risk and costs.

Introduction

As the next generation of transport aircraft evolves, it becomes much more difficult to improve aerodynamic performance as the limiting flow physics are being approached. Special topics of interest to the transport aircraft designer have become the laminar flow technology and the problem of engine/airframe integration, both promising large improvement potential in aerodynamic performance.

These aerodynamic problems with complex three-dimensional flow physics involved, can only be tackled by combining experiments in high quality aerodynamic test facilities and computational fluid dynamics (CFD) simulations.

A survey of CFD applications to turbofan/airframe integration shows a general trend towards more complex configurations and more accurate simulation of the flow physics involved, Fig. 1.

Investigations with three-dimensional panel codes reveal the strengths and weaknesses of linear potential methods. In the region of validity of the linear methods, i.e., subcritical flow, the results exhibit very good correspondence with experiments, especially if the codes are coupled with a prediction of the exhaust plume by a Navier-Stokes code.[1] Because no field grid has to be generated, which can be quite time consuming for complex configurations, panel methods offer the possibility to have a "quick look" at new configurations very early in the design cycle. However, transonic interference effects are not accurately simulated.

A quite sophisticated approach to overcome the limitations to subcritical flow is the so-called "hybrid-method."[2] It is based on the assumption that even in transonic flow the significant three-dimensional effects are linear in a first-order approximation. In consequence, the crossflow derivatives in the three-dimensional full-potential equation are determined by a three-dimensional panel calculation about wing/body/pylon/nacelle configurations including a jet model, whereas the remaining terms are resolved by a quasi two-dimensional full-potential finite difference code. The results are very promising, but the major limitation of this approach is that it is not applicable to supercritical crossflow and does not give reliable results close to the pylon.

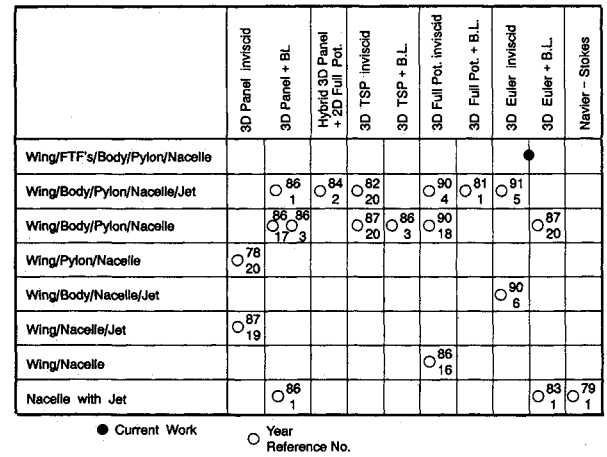

Fig. 1 CFD applications to engine/airframe integration.

Further developments in CFD have led to methods that are capable of resolving the details of the supercritical flow that might be present in the region of the engine installation and that can be applied to complete transport aircraft configurations.[3] Transonic small-pertubation (TSP) methods, however, lack the required geometric precision for wing/body/pylon/nacelle configurations because of the linearized wall boundary condition and can, therefore, only be used to investigate trends in configurational variations.

Applications of the more general full-potential equation to the problem of engine/airframe integration are widespread. The most common approach used to deal with the limitation of constant total pressure and temperature in the full-potential formulation is to use solid plume modeling as in some applications of three-dimensional panel methods. Just recently Chen et al.[4] introduced a new version of the TRANAIR full potential code that is capable of overcoming these shortcomings, and the applications of this code to isolated nacelles and installed engine/airframe combinations are impressive. The remaining restriction to isentropic shock-jump relations can be overcome if the flowfield is modeled by the Euler equations. The Euler equations allow regions of different total pressure and temperature and thus are dedicated for engine/airframe simulation with jet modeling. Further related contributions are indicated in Fig. 1 and can be found in Refs. 17–21.

As can be seen from Fig. 1, Navier-Stokes codes are not yet readily available for installed nacelle configurations, but

Presented as Paper 91-0025 at the AIAA 29th Aerospace Sciences Meeting, Reno, NV, Jan. 7–10, 1991; received Jan. 26, 1991; revision received June 19, 1991; accepted for publication July 28, 1991.

*Research Scientist, Theoretical Aerodynamics Branch. Member AIAA.

†Research Scientist, Theoretical Aerodynamics Branch.

for many installations viscous effects are not dominant such that the Euler equations, with some boundary-layer representation, are an adequate approach to simulate such complex flow physic phenomena like engine/airframe integration. This is shown by Rossow[5] as well as Ronzheimer et al.[6] and will be demonstrated in the following sections.

At Deutsche Airbus GmbH (DA) the Multiblock Euler integration algorithm MELINA together with the Interactive grid generation system INGRID,[7] both described in the following sections, and the Practical interactive solution analysis system PISA[8] for postprocessing form the tool package for three-dimensional inviscid compressible flow analysis.

The Euler code MELINA, based on the explicit, multiblock, cell-vertex Euler code CeVCATS developed at DLR,[9-11] is continuously being upgraded and adapted for the applications which are of interest to the transport aircraft designer at DA. In the multiblock approach the flowfield is partitioned into distinct zones, each discretized as a single grid block. This has several advantages over the single block concept:

1) The maximum storage space required is only corresponding to the maximum local grid block size.

2) Different types of grid topologies can be used in each block to improve mesh efficiency, hence the three-dimensional grid generation procedure becomes much easier, especially for complex configurations.

3) Different equation sets like Euler, Navier-Stokes, or boundary-layer equations can be used in different blocks to allow for the best physical representation in each zone of the flowfield.

With the interactive algebraic grid generator, INGRID, several tasks can be tackled. It serves as a geometry definition and manipulating system to create the configuration to be evaluated from given input data. At any stage of the construction user-defined curves describing the geometry can be graphically displayed for error-checking and judgment of the configuration. In a second step the surface is covered with a surface grid with full user control of the node distribution. Then a global multiblock mesh can be generated for a wing/body configuration. In order to add further components like pylon, engine, tail, etc., local blocks are then cut out of the global mesh and reconfigured corresponding to the components. Again, there are various options for interactive graphical display of the grid at any stage of the grid construction, and the user always has full control over grid spacing and distribution of the points.

In order to demonstrate the capabilities which have been achieved at DA, some aspects of the tool package will be presented for two modern transport aircraft configurations.

Three-Dimensional Grid Generation

Within INGRID the generation of three-dimensional grids around wing/fuselage combinations or even more complicated aerodynamic configurations is split into three steps 1) generation of a representation of the component's surfaces; 2) wrapping of a surface base mesh onto the components; and 3) generation of the three-dimensional space mesh. All essential functions are supported by graphics with mouse and menu technique, including the analysis of the input surface descriptions and detailed views of the three-dimensional mesh.

INGRID is based on the work of H. Sobieczky.[12] It has been enhanced by DA to an interactive tool for three-dimensional grid generation around configurations including wing, flap-track-fairings (FTFs), body, pylon, and engine. For wing/body combinations both C–H (C–O) and H–H (H–O) topologies are possible. Additional objects like engine, pylon, etc. are introduced using the local grid block technique which reconfigures one of the global blocks or a part of it to embed the new components of the configuration.

As the grid construction is based on algebraic functions, the computing time required for a complete three-dimensional mesh is very low. Thus INGRID allows the efficient construction of three-dimensional aerodynamic meshes on workstations in an interactive mode. Additionally, INGRID input data sets can be stored, instead of complete meshes which requires much less disk space.

Surface Definition

The first step of INGRID consists of a definition of objects and their relation to each other. The single components are defined in their own coordinate system and then translated to build the total configuration.

The wing is defined by span station airfoils and some functions along the plane wrap like geometrical twist, expected load twist, thickness, etc. The airfoils are given by sets of points, and they are splined along their arc length to redistribute the points according to the requirements from the flowsolver to be applied on the final mesh.

The pylon is constructed in a similar way, except that the airfoils do not fit to a constant spanwise station, but to a rotated coordinate system.

The airplane body is formed from simple, more or less double-elliptic, cross sections which can vary along the length of the body. The centerline of the fuselage is assumed to be straight so that the cross sections are all parallel.

The engine is treated as a full body which contains a second inner "body" to form the inner engine tube. In contrast to the airplane fuselage, both parts of this object follow a centerline which may be bended in the case of drooped nacelles.

The flap-track-fairings are also built by blending cross sections along a straight center line.

The surface meshes are the base meshes for the three-dimensional grid. They are constructed using the exact definition of the object's surfaces given above. Thus the three-dimensional mesh is always exactly aligned with the real surface of the configuration.

The major advantage of this included mini-CAD system for component construction appears in connection with airplane design. Prior to any time-consuming constructions or CAD descriptions of the new configuration, CFD results can be obtained and thus allow for a very early optimization in the design process. Interfaces to CAD systems are under development in order to ease the use of this system for already-defined configurations.

Space Meshes

The philosophy for the construction of three-dimensional multiblock meshes for complex configurations is a step-by-step one. Starting from a simple base configuration like a three-dimensional mesh around a wing/fuselage combination, more complex configurations are surrounded by a mesh using a cutout technique. Local blocks are cut out of the global mesh and filled with a new mesh that describes the additional components. Such a local block or local block system is required to fit to the boundaries of the cutout block.

The topology of the multiblock mesh around a certain configuration is defined in advance and cannot be changed by the user. Thus the difficulties with the topological definition of blocks and their relation to each other are already solved for a list of configurations and do not require too much insight from a design engineer. However, this strategy limits the system to special configurations, but fortunately, the number of different configurations is limited within a transport aircraft environment. It should be mentioned that it takes from about 2 weeks (adding winglets) to several months (adding pylon and engine) of programming and tuning to add completely new configurations to the list and optimize the grid for these "generic" new cases, depending on how massive the changes in block topology and aircraft configuration are.

Either a C–H(C–O) or an H–H(H–O) type mesh is possible as global mesh for wing/body combinations. The first one can only be used for wing/fuselage or wing alone calculations. The latter is the basis for wing-mounted or body-mounted engine configurations.

Two principle techniques are used to generate grid points in free space.

A one-dimensional curve construction algorithm is used to connect two points in three-dimensional space. The curve may start and/or end with a prescribed direction and a certain bending while the points on the curve are distributed following a given normalized distribution. The technique is a step-by-step one from one point on the curve to the next. In a first sweep it runs from point A to point B using v_A as start direction. The second sweep is reverse from B to A with v_B. A blending of both curves gives the result.

The second principal technique is for the generation of grid arrays in three-dimensional space. If the three-dimensional coordinate values are given on the boundary of a two-dimensional array of points, the inner values are distributed using a sophisticated blending of boundary arc length distributions. First an auxiliary straight line is calculated from one boundary to the opposite one. After that, the deviation of the given side boundaries from straight lines are blended and added to the auxiliary straight line. This technique can be applied even to very distorted arrays, also degenerated edges are allowed.

Simulation of Wing Boundary Layer

Inviscid flow simulation is not able to predict the spanwise load distribution of a wing correctly because the boundary-layer influence is not included. In the case of modern transport aircraft with rear loading wings, the viscous reduction of lift can amount up to 20 or 30% of the inviscid value.

The simplest way of boundary-layer consideration is a total lift adaptation by changing the angle of attack. But this method often leads to wrong load distributions and to a wrong location of the leading-edge attachment line, which is of essential importance for the prediction of laminar flow, for example.

Our approach to tackle the boundary-layer problem was along two paths:

In a first attempt we modified the wing with the boundary-layer displacement thickness that had been determined by a coupled three-dimensional full-potential/integral boundary-layer code.[13] Unfortunately, experimental and theoretical lift coefficients were still off by about 10% such that we pursued a second method which we call the "decambering method."

The spanwise load distribution for a certain flight situation is often known from experiment or can be very accurately predicted using simple (lifting surface) methods. It is known that calculations which are adapted to this distribution yield physically more accurate solutions. Our approach is to simulate the local decambering effect of the boundary layer along the wing span such that experimental and theoretical load distributions match. In each span section of the mesh, the wing airfoil is decambered and rotated in order to let the global angle of attack of the Euler calculation fit to the projected flight or wind-tunnel angle and to adapt the local lift and momentum coefficients to the predicted or measured local coefficients. This method is incorporated in the mesh generation program INGRID in such a way that the decambered airfoils serve as spanwise wing sections. The grid is then generated around the deformed wing.

Several tests have been performed to validate this technique. Using this decambering approach we are able to predict the flow over the wing very accurately with the Euler code MELINA. As an example of the simulation quality achieved, Fig. 2 shows a comparison of the experimental wing-section pressure distribution of a wing/body combination with a laminar flow wing and the corresponding Euler results with decambering and conventional angle-of-attack adaptation. The results reveal excellent correspondence of the decambered results and the experiment. At the trailing edge there are residual differences due to simulating only the decambering effect and not the displacement thickness of the boundary layer which is dominant at the very trailing edge.

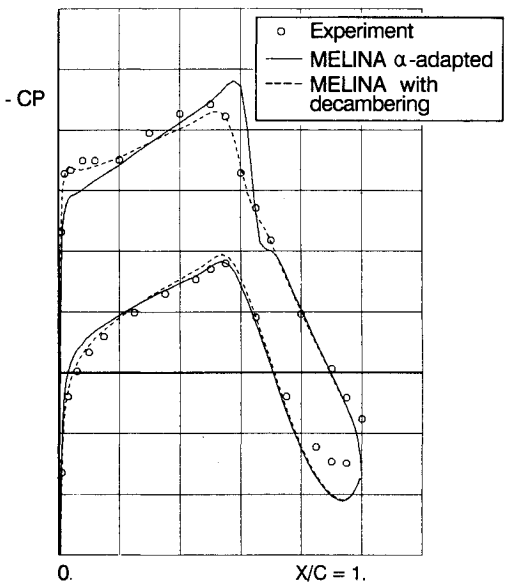

Fig. 2 Decambering effect on pressure distribution on laminar flow wing.

Conservation Equations for Inviscid Flow

Inviscid flow can be modeled by the continuum mechanic's conservation equations for mass, momentum, and energy. In three dimensions these are five scalar integral equations which are augmented by material laws to form a closed system. The caloric and thermic gas equations for ideal gas read

$$e = c_v T \qquad p = R\rho T = (\kappa - 1)\rho e \tag{1}$$

With this, for any control volume V the conservation of mass, momentum, and energy result in the system of Euler equations

mass

$$\frac{\partial}{\partial t}\int_V \rho \, dV = -\oint_{\partial V} \rho(\boldsymbol{v}\cdot\boldsymbol{n}) \, dO \tag{2}$$

momentum

$$\frac{\partial}{\partial t}\int_V \rho\boldsymbol{v} \, dV = -\oint_{\partial V} \rho\boldsymbol{v}(\boldsymbol{v}\cdot\boldsymbol{n}) + p\boldsymbol{n} \, dO \tag{3}$$

energy

$$\frac{\partial}{\partial t}\int_V \rho E \, dV = -\oint_{\partial V} \rho H(\boldsymbol{v}\cdot\boldsymbol{n}) \, dO \tag{4}$$

∂V is the surface of the control volume V, and $\boldsymbol{n}$ is the outward unit normal vector on ∂V.

According to Eq. (1) and the relation $E = e + (u^2 + v^2 + w^2)/2$ for the total energy, the pressure p can be calculated from

$$p = (\kappa - 1)\rho\left[E - \frac{u^2 + v^2 + w^2}{2}\right] \tag{5}$$

By definition the total enthalpy H is

$$H = E + \frac{p}{\rho} \tag{6}$$

Equations (2–4) can be abbreviated by the vector valued equation

$$\frac{\partial}{\partial t}\int_V \boldsymbol{W} \, dV = -\oint_{\partial V} \bar{\bar{F}}(\boldsymbol{W})\cdot\boldsymbol{n} \, dO \tag{7}$$

where $\bar{\bar{F}}$ is the flux tensor and $\boldsymbol{W} = (\rho, \rho u, \rho v, \rho w, \rho E)$ is the vector of dependent variables.

Cell Vertex Discretization

In order to discretize Eqs. (2–4), a boundary-fitted finite volume mesh, generated by INGRID, is used. In the cell vertex discretization the vertices of the finite volumes are taken as locations for the unknown variables $\boldsymbol{W}$. Following Jameson et al.[14] and others, the discretization by the method of lines decouples time and space directions. The discrete approximation of the flux integral on the right-hand side of Eq. (7) then results in a coupled system of five ordinary differential equations in time for any grid cell V.

The discretization of Eq. (7) leads to equations attached to finite volumes rather than grid points. Therefore a summation of the equations is applied which takes into account every eight cells connected to one common grid point. Thus the discretization of the flux integrals results in the equations

$$\frac{\partial}{\partial t}\int_{V_S} \boldsymbol{W}\,\mathrm{d}V = \sum_{l=1}^{8} Q_l \tag{8}$$

where

$$Q_l = -\oint_{\partial V_l} \bar{\bar{F}}(\boldsymbol{W})\cdot\boldsymbol{n}\,\mathrm{d}O \tag{9}$$

is the flux integral over cell no. l and $|V_S| = \Sigma_{l=1}^{8} |V_l|$ is the volume of the supercell constructed from the participating grid cells. This kind of scheme is also used by Ni[15] and Hall.[16]

According to the instationary Euler equations the flux integral can be understood as the integral mean value of the temporal change of the dependent variables $\boldsymbol{W}$:

$$Q_l = \frac{\partial}{\partial t}\int_{Vl} \boldsymbol{W}\,\mathrm{d}V = \int_{Vl}\frac{\partial \boldsymbol{W}}{\partial t}\,\mathrm{d}V_l = \left|V_l\right|\left.\overline{\frac{\partial \boldsymbol{W}}{\partial t}}\right|_l \tag{10}$$

If Q_l in Eq. (8) is replaced by this expression, Eq. (8) is the volume-weighted supercell integral equation definition presented by Hall[16] and Rossow.[9]

Equation (8) is not stable in the sense that the stationary solution admits oscillatory components which are not physically correct. Therefore it is necessary to eliminate these components from the solution. In the context of central difference schemes this is usually done by adding an appropriate filter term to the system of equations. This artificial filter or dissipation consists of two parts: The so-called background dissipation is necessary to ensure convergence for the whole range of flow speeds to be treated. In Jameson's approach[14] it consists of undivided fourth differences of the solution vector multiplied by an approximation of the largest eigenvalue of the Jacobian matrix $\partial\bar{\bar{F}}/\partial\boldsymbol{W}$ and a user-defined constant $\varepsilon^{(4)}$. The second dissipation term is an undivided second difference. It is designed to avoid oscillations of the solution near shocks and is switched on only in those regions by the use of a special pressure-based sensor function.

The time discretization depends on the treatment of the volume integral in Eq. (8). In our case a hybrid, explicit five-stage Runge-Kutta time-stepping scheme is chosen where the integral is defined by the relation

$$\frac{\partial}{\partial t}\int_{V_S} \boldsymbol{W}\,\mathrm{d}V \approx \left|V_S\right|\left.\frac{\partial \boldsymbol{W}}{\partial t}\right|_{\text{centre}} \tag{11}$$

For convergence acceleration additional techniques like local time-stepping, implicit residual averaging, and enthalpy-damping (in the case of no enthalpy jump in the jet) are used.

Boundary Conditions

In the block-structured mesh used for three-dimensional complex configurations various boundary condition types exist. First the physical boundaries of the computational domain will be treated. The computational domain may be bounded by solid walls, the far field, fan face, and exhaust planes of the engine and the symmetry plane if one exists.

On a solid body the velocity component normal to the wall is zero. Hence, the flux integral parts along the faces of the control volume that are aligned with the body reduce to the pressure integrals of the momentum equations:

$$\oint_{\partial\text{body}} \bar{\bar{F}}(\boldsymbol{W})\cdot\boldsymbol{n}\,\mathrm{d}O = \begin{pmatrix} 0 \\ \oint_{\partial\text{body}} p\cdot\boldsymbol{n}\,\mathrm{d}O \\ 0 \end{pmatrix}$$

In contrast to cell-centered codes, the pressure on the body is already defined. No special relation for the evaluation of the pressure on the wall is necessary.

The computational domain is bounded by an artificial far-field boundary where some special boundary conditions have to be imposed. On one hand, these conditions have to bring the information of the undisturbed flow into the computational domain. On the other hand, they have to let pass disturbances emanating from the model into the freestream without reflection. The theory of characteristics, which can be applied to the hyperbolic locally linearized system of Euler equations, leads to a set of conditions for the characteristic variables. A transformation of these variables to the dependent variables $\boldsymbol{W}$ used in the rest of the flowfield results in proper equations for the values of $\boldsymbol{W}$ at the outer boundary.

The boundary condition of symmetry is enforced with the use of guard cells which are mirror images of the cells abutting the symmetry plane.

The boundary condition at the fan face should yield the mass flow specified by the engine data at the flow condition to be evaluated. The mass flow at the fan face of the engine is defined as

$$\dot{m}_{\text{Fan}} = \rho_{\text{Fan}} q_{\text{Fan}} A_{\text{Fan}} \tag{12}$$

which can be expressed in terms of Mach number at the fan M_{Fan}, stagnation density and stagnation temperature of the undisturbed flow

$$\dot{m}_{\text{Fan}} = A_{\text{Fan}} M_{\text{Fan}} \left(1 + \frac{\gamma-1}{2} M_{\text{Fan}}^2\right)^{-(\gamma+1)/(2(\gamma-1))} \rho_t \sqrt{\gamma R T_t} \tag{13}$$

The last equation can be solved iteratively for M_{Fan}. Temperature and density, as well as static pressure at the fan face can then be determined from isentropic relations. These data are used to determine the boundary condition at the fan face using the same characteristic procedure as in the case of the farfield condition.

The boundary condition at the exit of the engine has to be formulated such that the jump in stagnation pressure and stagnation temperature given in the engine data is realized. Using isentropic relations and one-dimensional energy conservation, ρ and p can be computed from stagnation density, stagnation temperature, and magnitude of velocity at the exhaust plane q_{Ex}

$$\rho_{\text{Ex}} = \rho_{t_{\text{Ex}}} \left(1 + \frac{\gamma-1}{2}\frac{q_{\text{Ex}}^2}{\gamma R T_{t_{\text{Ex}}} - \frac{\gamma-1}{2} q_{\text{Ex}}^2}\right)^{-1/(\gamma-1)} \tag{14}$$

$$p_{\text{Ex}} = p_{t_{\text{Ex}}} \left(\frac{\rho}{\rho_{t_{\text{Ex}}}}\right)^{\gamma} \tag{15}$$

This relation is assumed to apply on the whole exit plane. According to the theory of characteristics, four conditions have to be specified, and one condition is extrapolated from the interior of the computational domain if the exhaust Mach

number M_{Ex} is subsonic. Therefore, q_{Ex} is extrapolated from the interior; pressure and density are determined by Eqs. (14) and (15). The direction of the jet at the exhaust plane is defined to be parallel to the x axis, i.e., $v = 0$ and $w = 0$.

The second group of boundary condition types is related to the algorithmic boundaries between grid blocks. In the present code various boundary condition types of this category are implemented. These inner-cut conditions manage the exchange of grid coordinates and solution at the nodes from one block to the other, depending on the type of blocks that have a common block segment. Practically, this is done by introducing guard cells for each block face which leads to an overlapping of blocks that are divided by an inner cut. In the simple case with a one-to-one correspondence of points on both abutting block faces, the grid coordinates and data at the nodes are simply copied from the corresponding cell of the neighboring block to the guard cell.

In order to optimize the distribution of nodes, the options of enrichment and coarsening from one block to an other have been implemented. Enrichment means the splitting of each finite volume into two in each desired coordinate direction and linear interpolation of the coarse node data, whereas in the case of coarsening, every other grid node is dropped in the specified direction.

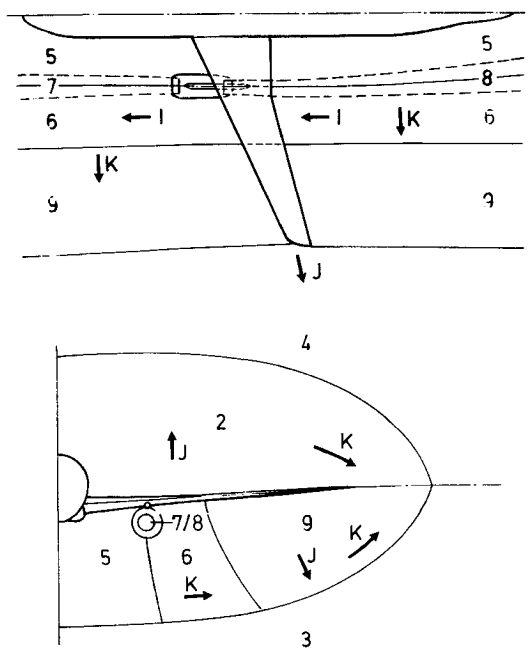

Fig. 3 Global grid block topology of body/wing/pylon/nacelle configuration.

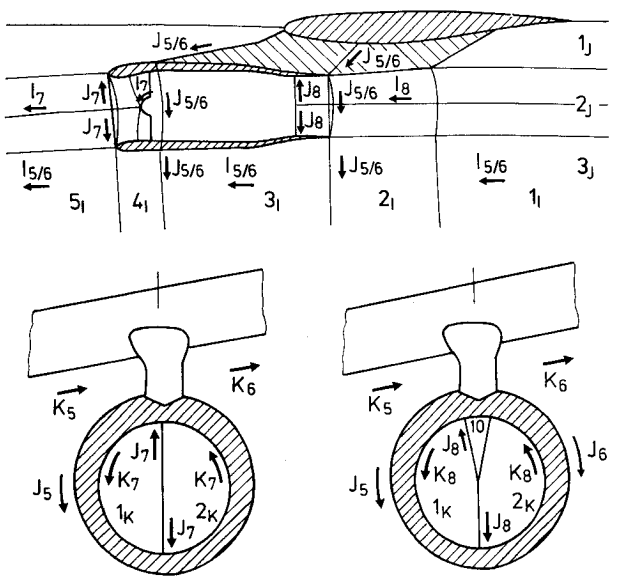

Fig. 4 Grid block topology of body/wing/pylon/nacelle configuration near the engine.

Numerical Results

The CFD system described above is among other applications used to analyze the problems arising with engine/airframe integration. The main purpose of this investigation is to show whether the engine installation effects can be predicted by the numerical simulation of the flowfield with MELINA. Three different calculations are compared with each other and with wind tunnel measurements 1) body/wing configuration, 2) body/wing/pylon/nacelle configuration, and 3) body/wing/FTFs/pylon/nacelle configuration of a modern transport aircraft.

Before the results will be presented and discussed it is worthwhile having a look at the grid block topology used for these computations. For the body/wing/pylon/nacelle case, the grid consists of 9 blocks which can be identified in Fig. 3 and Fig. 4 as blocks 2–10. Blocks 2–4 are identical with the blocks of the body/wing configuration. Grid block 9 consists of the remaining part of former block 1 which was not cut-out for rearrangement, whereas blocks 5, 6, 7, 8, and 10 result from rearranging the body/wing-block 1 according to the cut-out technique. Grid blocks 7 and 8 form the nacelle inlet and exit tubes which extend to the far field up- and downstream. Block 10 is a special block that had to be introduced, because the pylon extends over the nacelle rear end into the jet.

In order to achieve good spacial resolution in the region of pylon and nacelle without vasting points in other regions, the technique of enrichment and coarsening from one grid block to the other has been used extensively. The far field blocks 3 and 4 (see Fig. 3) are coarsened in i and k direction relative to blocks 2, 5, 6, and 9. Block 2 on the upper wing side is only half as fine in j direction as blocks 5, 6, and 9 on the lower wing side.

Although the number of points could be reduced significantly with the coarsening and enrichment strategy, it was found that an overall number of 950,000 grid points are necessary for a sufficient spacial resolution in the body/wing/pylon/nacelle case, corresponding to 146 points around each of 45 spanwise airfoil sections. Generating this mesh on a DN4000 Apollo Workstation takes 15 min with the INGRID mesh generation system. To run the Euler code on a Fujitsu VP200 vector supercomputer takes 2 h of CPU time for the

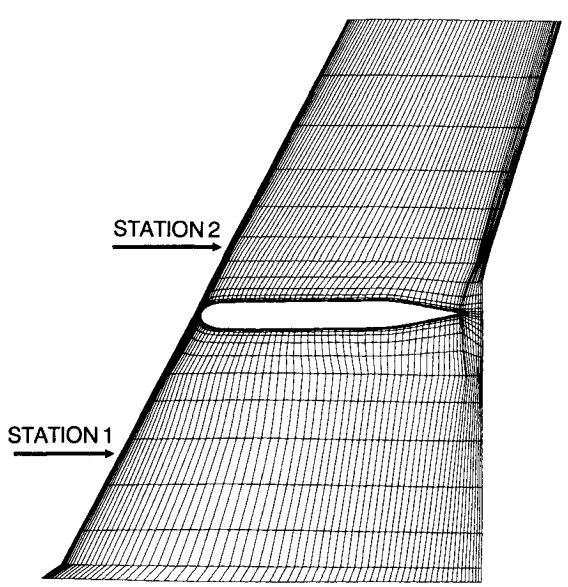

Fig. 5 Spanwise stations of pressure tabs and surface grid on lower wing side.

body/wing case and about 2.5 h for the body/wing/pylon/nacelle configuration to converge.

The spanwise stations, at which experimental pressure data near the pylon were available, are depicted in Fig. 5 together with the surface grid on the lower wing side. In Figs. 6 and 7 a comparison of the computed pressure distributions for the configuration with and without pylon and nacelle and the corresponding experimental data are presented.

The theoretical and experimental results show a good correspondence in all cases; remember the code is inviscid. The flow at the leading edge is modeled with high accuracy which is a consequence of the correct angle of attack in the Euler calculation. The residual discrepancies between experiment and simulation occur in the region behind the shock, at the lower wing side and at the trailing edge. The problems at the shock (shock boundary-layer interaction) and the trailing edge are a consequence of the lacking boundary-layer thickness modeling in the code, whereas the differences at the lower wing side mainly result from FTFs that had been mounted on the wing in the experiment and were not modeled in this particular simulation.

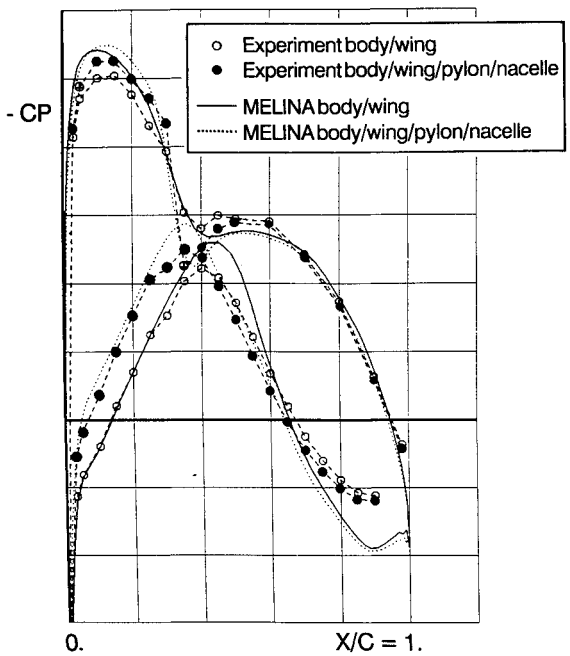

Fig. 6 Comparison of pressure distributions at station 1.

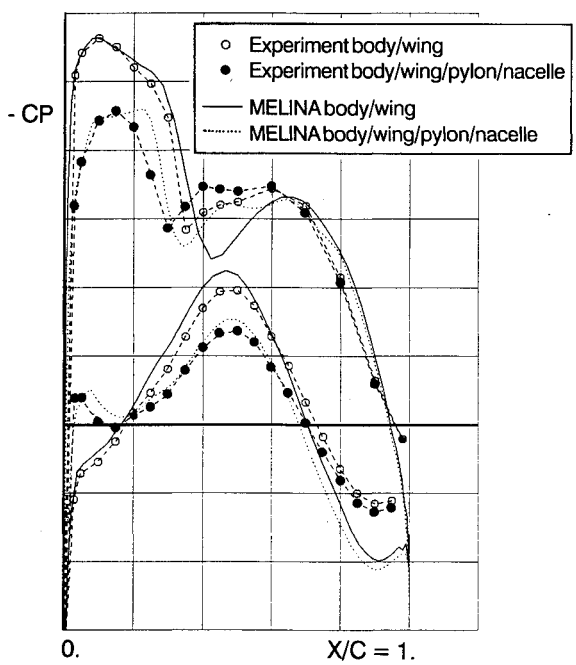

Fig. 7 Comparison of pressure distributions at station 2.

In order to find out whether the engine installation effects are predicted accurately with the Euler code MELINA, the pressure distribution of the engine mounted configuration and the clean wing case were subtracted from each other. This was done for the theoretical and experimental data at the measuring stations and plotted in Figs. 8 and 9. It was expected that due to the subtraction the uncertainties inherent in the method (simplified viscous effects) and the experiment could be eliminated and that the effect of the FTFs which were not present in the numerical simulation, but on the wind-tunnel model, could be filtered out.

In Figs. 8 and 9 positive and negative cp values correspond to deceleration and acceleration of the flow due to the engine installation respectively. There is an astonishingly good correlation between theory and experiment. At the inboard station the engine installation has a different effect than outboard of the pylon. Inboard the flow at the upper wing side is affected not very much except at the bottom of the shock. At the lower wing side there is a strong acceleration to almost 40% of the chord due to the "tunnel"-effect between fuselage and pylon. This behavior changes if we look at the outboard station, Fig. 9, where the flowfield at the upper wing side is largely affected. Further investigations of the flowfield have shown that the interference between wing, pylon, and nacelle

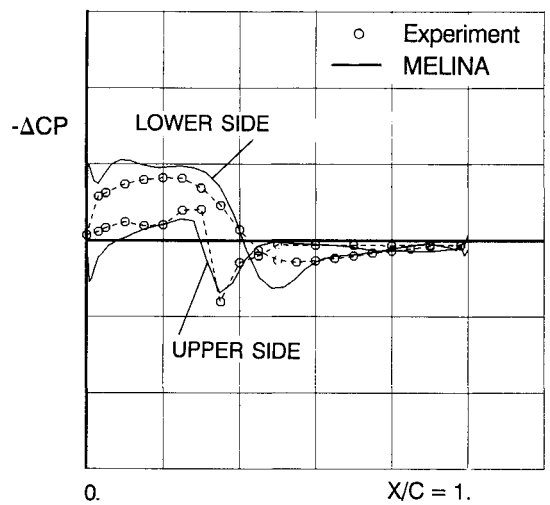

Fig. 8 Engine installation effects at station 1 (Δcp: = $cp_{\text{engine-mounted}} - cp_{\text{clean}}$).

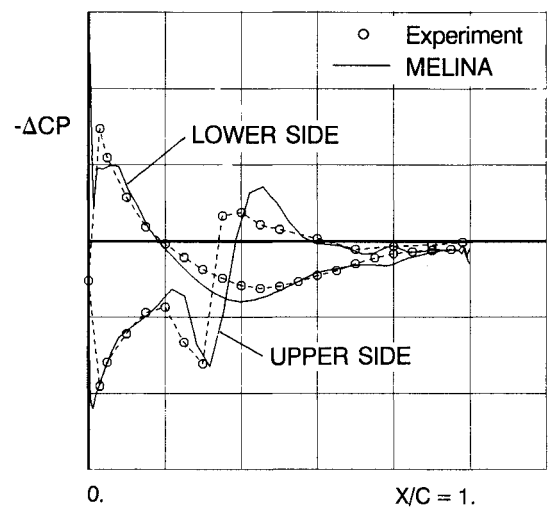

Fig. 9 Engine installation effects at station 2 (Δcp: = $cp_{\text{engine-mounted}} - cp_{\text{clean}}$).

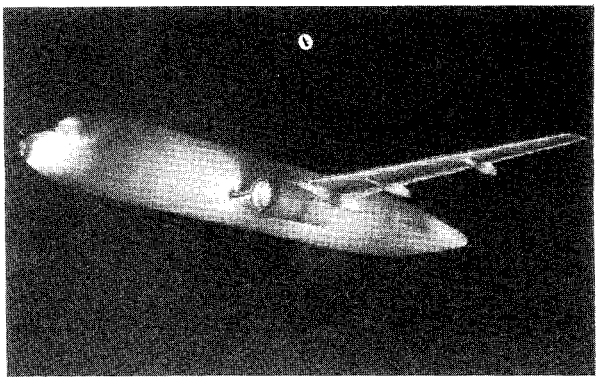

Fig. 10 General arrangement and pressure distribution on body/wing/ftfs/pylon/nacelle.

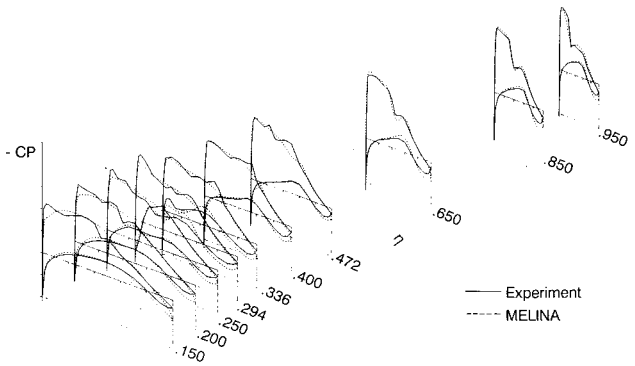

Fig. 11 Wing pressure distribution for body/wing/ftfs/pylon/nacelle case.

is strongly influenced by the crossflow component. For the test case presented, this leads to the fact that installation effects almost cancel each other at the inboard upper wing side but are adding up at the outboard upper wing side.

Because of the close coupling of FTFs, wing, pylon, and engine, some interference was expected due to the presence of FTFs. During the investigation this lead to a generalization of the surface definition and grid generation with respect to the implementation of FTFs. Fig. 10 shows the general arrangement of a transport aircraft configuration with FTFs, pylon, and nacelle. Onto the surface the distribution of the negative! pressure coefficient is projected. This type of illustration can only serve for qualitative judgment of the solution to locate discretization errors and to get a general impression of the solution. Much more information about the quality of the simulation can be drawn from a comparison of the wing pressure distribution shown in Fig. 11.

Conclusions

The MELINA Euler code in connection with the INGRID mesh generation system has proven to allow for accurate inviscid flow simulations around complex aircraft configurations of body/wing/flap-track-fairing/pylon/engine type. A multiblock structured grid with sufficient grid control can be generated on a workstation using algebraic techniques. This grid is input to the general multiblock Euler code which can handle relatively arbitrary block topologies. The results obtained for a twin-jet transport airplane exhibit good comparison with measurements and allow use of the system to optimize the aerodynamical design of the engine installation.

References

[1]Tinoco, E. N., and Chen, A. W., "CFD Applications to Engine/Airframe Integration," *Numerical Methods for Engine-Airframe Integration,* Progress in Astronautics and Aeronautics, Vol. 102, AIAA, New York, 1986, pp. 219–255.

[2]Ehrmann, M., Klevenhusen, K. D., Rudolph, K., and Burgsmüller, W., "Computation of Engine/Airframe Interference Flows at Subsonic and Transonic Speeds," International Council of the Aeronautical Sciences, Paper 84-2.10.1, Toulouse, 1984.

[3]Yaros, S. F., Carlson, J. R., and Chandrasekaran, B., "Evaluation of Three Num. Methods for Propulsion Integration Studies on Transonic Transport Configurations," NASA-TM-87727, June 1986.

[4]Chen, A. W., Curtin, M. M., Carlson, R. B., and Tinoco, E. N., "TRANAIR Applications to Engine/Airframe Integration," *Journal of Aircraft*, Vol. 27, No. 8, 1990, pp. 716–721.

[5]Rossow, C. C., "Computation of Inviscid Flow Fields Around Complex Configurations Using a Multiblock Multigrid Method," *Fifth Copper Mountain Conference on Multigrid Methods*, Colorado, USA, March 31–April 5, 1991.

[6]Ronzheimer, A., Rossow, C. C., and Pflug, M., "Untersuchungen zum Interferenzeinfluß von modernen Hochbypass-Antriebskonzepten an einer Flügel-Rumpf Kombination durch Lösung der Eulergleichungen," *DGLR Jahrestagung*, Paper 90–108, Oct. 1990.

[7]Becker, K., "Interactive Algebraic Mesh Generation for Twin Jet Transport Aircraft," in *Proceedings of the Third International Conference on Numerical Grid Generation*, Barcelona, June 1991.

[8]Becker, K., and Rill, S., "Practical Interactive Solution Analysis—the PISA System," DA-report (submitted for publication).

[9]Rossow, C. C., "Berechnung von Strömungsfeldern durch Lösung der Euler-Gleichungen mit einer erweiterten Finite-Volumen Diskretisierungsmethode," DLR Rept. FB 89–38, 1989.

[10]Radespiel, R., and Rossow, C., "Konvergenzbeschleunigung bei der Berechnung der reibungsfreien Umströmung eines Tragflügels," DGLR-Bericht 88–05, 1989, pp. 301–312.

[11]Kroll, N., Rossow, C. C., Scherr, S., Schöne, J., and Wichmann, G., "Analysis of Three-Dimensional Aerospace Configurations Using the Euler Equations," AIAA Paper 89-0268, 1989.

[12]Sobieczky, H., "Geometry Definition and Grid Generation for Wing-Fuselage Configurations and Turbomachinery Components," DFVLR Rept. IB 221-86/A20, 1987.

[13]Wichmann, D., and Zhang Zhong-Yin, "Calculation of Three Dimensional Transonic Wing Flow by Interaction of a Potential and an Integral Boundary Layer Method," DFVLR Rept. IB 129-89/12, 1989.

[14]Jameson, A., Schmidt, W., and Turkel, E., "Numerical Solutions of the Euler Equations by Finite Volume Methods Using Runge-Kutta Time Stepping Schemes," AIAA Paper 81-1259, 1981.

[15]Ni, R. H., "A Multiple Grid Scheme for Solving the Euler Equations," AIAA Paper 81-1025, 1981.

[16]Hall, M. G., "Cell Vertex Multigrid Schemes for Solution of the Euler Equations," *Numerical Methods for Fluid Dynamics II*, edited by K. W. Morton and M. F. Baines, Oxford Science Publications, Oxford, England, 1986.

[17]Atta, E. H., and Vadyak, J., "Numerical Simulation of the Transonic Flowfield for Wing/Nacelle Configurations," *Journal of Aircraft*, Vol. 23, No. 1, 1986.

[18]Lord, W. K., and Zysman, S. H., "VSAERO Analysis of a Wing/Pylon/Nacelle Configuration," AIAA Paper 86-1523, 1986.

[19]Mirat, J. J., Perin, R., and Castan, C., "Engine Installation Design for Subsonic Transport Aircraft," International Council of the Aeronautical Sciences, Paper 90-2.7.4, Stockholm/Sweden, 1990.

[20]Sauer, G., and Szodruch, J., "Untersuchung des Triebwerkeinflusses an Flügeln mit modernen Hochbypass-Antriebskonzepten," *DGLR-Jahrestagung*, Berlin, 1987.

[21]Tinoco, E. N., "CFD Applications to Complex Configurations: A Survey," *Applied Computational Aerodynamics,* Progress in Astronautics and Aeronautics, Vol. 125, AIAA, New York, 1990, pp. 559–615.